Understanding the effect of density functional choice and van der Waals treatment on predicting the binding configuration, loading, and stability of amine-grafted metal-organic frameworks

Jonathan R. Owens,[1, a)] Bojun Feng,[2, a)] Jie Liu,[1] and David Moore[3]
[1)]*Material Chemistry and Physics Lab, GE Vernova Advanced Research, Niskayuna, NY*
[2)]*AI, Software, and Robotics Lab, GE Vernova Advanced Research, Niskayuna, NY*
[3)]*Decarbonization Lab, GE Vernova Advanced Research, Niskayuna, NY*

(*Electronic mail: Jon.R.Owens@ge.com)

(Dated: 7 February 2024)

Metal organic frameworks (MOFs) are crystalline, 3-dimensional structures with high surface areas and tunable porosities. Made from metal nodes connected by organic linkers, the exact properties of a given MOF are determined by node and linker choice. MOFs hold promise for numerous applications, including gas capture and storage. M_2(4,4'-dioxidobiphenyl-3,3'-dicarboxylate) - henceforth simply M_2(dobpdc), with M = Mg, Mn, Fe, Co, Ni, Cu, or Zn - is regarded as one of the most promising structures for CO_2 capture applications. Further modification of the MOF with diamines or tetramines can significantly boost gas species selectivity, a necessity for the ultra-dilute CO_2 concentrations in the direct-air capture (DAC) of CO_2. There are countless potential diamines and tetramines, paving the way for a vast number of potential sorbents to be probed for CO_2 adsorption properties. The number of amines and their configuration in the MOF pore are key drivers of CO_2 adsorption capacity and kinetics, and so a validation of computational prediction of these quantities is required to suitably use computational methods in the discovery and screening of amine-functionalized sorbents. In this work, we study the predictive accuracy of density functional theory (DFT) and related calculations on amine loading and configuration for one diamine and two tetramines. In particular, we explore the Perdew-Burke-Ernzerhof (PBE) functional and its formulation for solids (PBEsol) with and without the Grimme-D2 and Grimme-D3 pairwise corrections (PBE+D2/3 and PBEsol+D2/3), two revised PBE functionals with the Grimme-D2 and Grimme-D3 pairwise corrections (RPBE+D2/3 and revPBE+D2/3), and the non-local van der Waals correlation (vdW-DF2) functional. We also investigate a universal graph deep learning inter-atomic potential's (M3GNet) predictive accuracy for loading and configuration. These results allow us to identify a useful screening procedure for configuration prediction that has a coarse component for quick evaluation and a higher accuracy component for detailed analysis. Our general observation is that the NNP can be used as a high-level and rapid screening tool, whereas PBEsol+GD3 gives a completely qualitatively predictive picture across all systems studied, and can thus be used for high accuracy motif predictions. We close by briefly exploring the predictions of relative thermal stability for the different functionals and dispersion corrections.

I. INTRODUCTION AND MOTIVATION

Among the numerous materials being considered for solid CO_2 sorbents, metal-organic frameworks (MOFs) are some of the most promising[1–3]. Through tuning the substituent metal nodes and organic linkers, these highly crystalline materials allow altering of their surface areas, pore sizes, and open metal sites to optimize their structural and adsorption properties. MOFs also show promise for, e.g., capture of other gases[4,5], energy storage[6,7], and drug delivery[8], and so the research community has intensively investigated this class of materials. In 2020, it was estimated that there are over 90,000 MOFs synthesized and 500,000 theorized[9], giving way to an enormous search space for finding the optimal structure for a particular application.

For CO_2 capture applications, an ideal MOF will exhibit structural stability, be robust to thermal fluctuations and contaminant molecules, and display high species selectivity for CO_2. In the direct-air capture (DAC) of CO_2, where concentrations are around 400ppm[10], selectively adsorbing only CO_2 is critical for deployable systems. There are numerous different mechanisms for tuning a material to be highly selective for CO_2[11], including gating of the kinetic diameter[12], geometry gating[13], and amine-functionalization[14]. The latter approach is the focus of this paper. In this situation, an environment exists that selectively allows the adsorption of CO_2 via a chemical bond[15–18], so-called chemisorption.

Amine functionalization refers to the attachment of amines to the open metal sites of the MOF. This can be physically realized by soaking a M_2(dobpdc) preparation in amine solution[15,19]. There are different classes of amines being studied for carbon capture applications, most commonly diamines[15,17,18,20–24] (wherein the molecule has two amine groups) and tetramines[19] (wherein the molecule has four amine groups). This enhanced capability comes with an increase in complexity and size of the search space. The need to predict, from first principles, the structure of a hypothetical MOF + amine combination is thus crucial for material discovery.

There is a wealth of experimental[14,15,17,19–26] and theoretical[26–32] literature exploring the fundamentals of the chemisorption process. The general understanding is that CO_2 adsorption in amine-functionalized MOFs mostly manifests in

[a)]These two authors contributed equally

the form of insertion of CO_2 between the metal node and primary amine, with proton transfer and the formation of ammonium carbamate chains[15,17,19,21,28,33], causing step-shaped isotherms, and thus greater working capacity with smaller temperature or pressure swings. The other predominate chemistry is carbamic acid formation[17,33], assumed to be in pairs on the secondary amines. With these chemistries, the maximum theoretical capacity is 1 CO_2 molecule per diamine or 2 CO_2 molecules per tetramine. As such, an accurate prediction of amine loading (i.e., how many amines can fit in the unit cell of a MOF) allows predicting maximum sorbent capacity. A particular configuration of an amine in the pore (a so-called motif) also influences the stability, pore volume, and binding energy.

All of this leads to the inevitable conclusion that being able to accurately predict the motif and loading of a hypothetical MOF and amine combination is required to make accurate predictions of a sorbent's CO_2 capture performance. Prior work by Lee, *et al.* shows large changes in quantitative predictive quality for various functionals and van der Waals schemes for CO_2 adsorption energies[34]. In this work, we evaluate the predictive accuracy of the density functional choice and dispersion corrections on amine configuration and loading. Though we are studying structures with known configurations, we approach each structure how we would study it if we had no knowledge of the true motif.

We systematically study one diamine[34] and two tetramines[19] with crystallographically well-defined experimental structures, giving 3 starting motifs. We additionally draw hypothetical motifs that one might predict if they had not known the structure. The experimental structures, combined with some drawn alternatives, give a total of 6 motifs. See Figures 1, 3, and 8. For every motif, we study the binding energy of a single amine in the MOF pore and the average binding energy of a fully loaded system for that configuration. In each of these 12 systems, we evaluate the relative energetics for 11 different functional/dispersion corrections[35–43], as well as structural relaxations with atomic interactions parameterized by a neural network potential (NNP)[44], M3GNet, to determine the predicted loading and configuration.

The goal of this paper is to identify a framework for accurately and reliably predicting amine binding and loading configuration, thereby giving trustworthy predictions of structures as a starting point for further computational study. The rest of the paper is structured as follows: Section II outlines our methods for hypothesizing structural motifs, discusses the density functional theory calculations performed and functionals and non-local effects considered, gives an overview of the neural network potential (NNP) used, and finally defines the adsorption energy formulae used in the subsequent evaluations. Section III gives the computed results for the different materials and methods, with detailed discussions of the results and difference in the subsection of each unique material. Section IV gives a higher-level, conceptual discussion and interpretation of the results presented in the previous section. It also offers a potential screening pipeline for a novel material. Finally, Section V contains a brief discussion of thermal stability predictions from the amine binding strength. In the Supplemental Information (Section VII A), the performance of the different functionals and dispersion corrections with respect to thermal stability via *ab initio* molecular dynamics calculations is outlined.

II. METHODS

A. Structures

The magnesium variant of M_2(dobpdc) (Mg_2(dobpdc)) is the most promising for CO_2 adsorption applications, but it is difficult to obtain a well-resolved single-crystal structure[19]. Most crystallographically resolved structures are thus for the zinc variant, Zn_2(dobpdc)[19]. For the remainder of this paper, we will be discussing different amines and their configurations on this base MOF of Zn_2(dobpdc). Generally speaking, M_2(dobpdc) with different metal species are known to be isostructural[19].

The initial motifs for all three amines were extracted from publicly available CIFs[19,34]. Based on the size and nature of the amine, different possible configurations in the pore were hypothesized. For *N,N'*-dimethylethylenediamine, we simply rotated the diamine by 90 degrees to point along the crystallographic *c*-axis. This decision is discussed in Section III A. For norspermine (*N,N'*-bis(3-aminopropyl)-1,3-diaminopropane), the general flexibility of the molecule gives rise to different configurations of the gaseous phase. We chose two: one was the linear configuration, which is what one would get if they downloaded the molecular coordinates on ChemSpider[45], and the other was the 'S-shaped' configuration, which is observed in the bound state in the pore[19]. For spermine (*N,N'*-bis(3-aminopropyl)-1,3-diaminobutane), we studied the sole gaseous configuration to be the mostly linear one, which again is close to what is observed in the experimental structure[19]. These different structures allow 8 unique motifs.

The drawn structures were initially generated via manual insertion with Avogadro[46,47], then coarsely relaxed using M3GNet[44] in the Atomic Simulation Environment[48]. From these coordinates, we applied the space group symmetries to the pre-relaxed structure to fill the pore more accurately (and less tediously) than drawing the amines at the equivalent sites. For each motif, we consider two situations: one in which a single amine binds and one in which we look at the average binding energy of a fully loaded pore.

B. Density functional theory calculations

DFT calculations were performed with GPU-accelerated Quantum ESPRESSO[49–51], version 7.2. A plane wave cutoff of 85 Ry (1156 eV) and Monkhorst-Pack sampling[52] of $1 \times 1 \times 2$ *k*-point grid for structures with only one *c*-repetition and $1 \times 1 \times 1$ grid for structures with more than one *c*-repetition gave converged energies within 0.001 Ry (2 kJ/mol). The structures were relaxed in a variable cell scheme to have forces less than 0.0001 Ry/Bohr (0.002 eV/Å) and

$\Delta E_{\text{tot}} < 0.00084$ Ry (1 kJ/mol). The tetragonal symmetry of the structure was retained, as the angles between the crystallographic axes were kept fixed, but the magnitudes of the cell parameters ($|a| = |b|, |c|$) were varied.

A mixture of plane-augmented wave (PAW)[53] and ultrasoft (US) pseudopotentials[53–56] were used, depending on the particular calculation. US pseudopotentials were used in the Grimme-D2 calculations, as these served as the starting point for our AIMD runs, which can only use US pseudopotentials, as implemented in Quantum ESPRESSO.

CIF input files for the initial structures from the literature, and subsequently drawn structures, were converted into the PWscf input format using the Materials Cloud tool provided by the Materials Project[57].

1. *Functionals*

We here want to understand how variations in functional choice and van der Waals treatment affect the qualitative and quantitative prediction of *amine* binding energy, and how that affects the predicted loading and motif. We explore the Perdew-Burke-Ernzerhof (PBE) functional[37] and its formulation for solids (PBEsol)[40] with and without the Grimme-D2[41] and Grimme-D3[42] pairwise corrections (PBE+D2/3 and PBEsol+D2/3), two revised PBE functionals[38,39] with the Grimme-D2 and Grimme-D3 pairwise corrections (RPBE+D2/3 and revPBE+D2/3), and the non-local van der Waals correlation (vdW-DF2) functional[43].

Ordinary PBE was chosen because of its status as the standard GGA functional, as well as its accurate prediction of CO_2 chemisorption energies[34]. PBEsol was designed to give some improvements in packed solid systems and surface energies[40]. RPBE and revPBE were developed to specifically improve chemisorption energies[38,39], and also were observed to give the best compromise between structural parameters and chemisorption energies in diamine-functionalized MOFs[34]. Lastly, vdw-DF2 was selected as a representative fully non-local functional, with density dependence of the non-local correlation (Eq. 12). This functional has also been used in other works studying both chemisorption[19,24] and physisorption[58,59]. A more detailed discussion of the different functionals and how their form affects the predicted binding motifs can be found in Section IV.

2. *van der Waals*

Stefan Grimme and colleagues[60] have a thorough review of dispersion-corrected mean-field electronic structure methods, discussing the relative benefits and drawbacks of various approaches for different applications. For our case of MOFs, there are existing systematic studies of CO_2 adsorption in MOFs considering different dispersion corrections[61]. Early work considered physisorption on bare M-MOF74[58,59,61]. More recently, work by Lee, *et al.* performed a similar study on the chemisorption of diamine-functionalized MOFs[34]. Surprisingly, this work reported the standard PBE functional gives accurate CO_2 binding energies and enthalplies in diamine-functionalized MOFs, though gave less accurate lattice parameters. Regardless, it is generally expected that some form of van der Waals consideration must be used to accurately understand amine-appended MOFs and their potential as chemisorbents[61].

The Grimme D2 scheme provides an empirical dispersion correction to the DFT energy[41], and the D3 scheme improves this method by adding higher order corrections to the energy[42], and by taking the chemical environment of a particular ion (i.e., its coordination number) into account. The vdW-DFx methods, like vdW-DF2 explored here, explicitly account for a density dependent non-local correlation term. The mathematical form of these methods, and a deeper discussion of them, can be found in Section IV C.

C. Neural Network Potentials (NNP)

Neural network potentials (NNPs) have recently become a vital component of the computational materials toolkit[44,62,63]. They are used to parameterize the potential energy surface (PES) of an atomic system by leveraging machine learning techniques to model it as a function of local environment descriptors. NNPs generally achieve superior accuracy in computed energies and forces compared to traditional inter-atomic potentials, while also facilitating precise and efficient simulations over length and timescales that exceed the capabilities of *ab initio* methods. Graph neural networks (GNNs) enable a natural representation of molecules and crystals, wherein nodes and edges represent atoms and the bonds between them. We use a GNN trained by the Materials Project[64], the Materials 3-body Graph Network (M3GNet) architecture[44]. It is trained on more than 187,000 energies, 16,000,000 forces and 1,600,000 stresses from DFT structural relaxations using PBE or the GGA+U method and is applicable for 89 elements of the periodic table with low energy, force and stress errors. It can be used for structural relaxations, molecular dynamics simulations, *etc*. M3GNet's training set does not include van der Waals effects, and so the computed binding energy deltas we consider will likely be weaker (less negative). In our work, a slight improvement is made to the M3GNet source code to enable structural relaxation of crystal structures with fixed cell symmetry while both the cell volume and atomic positions of atoms are allowed to move.

D. Amine binding energy calculations

The single amine binding energy is calculated as

$$\Delta E_{\text{ads}} = E_{\text{MOF+amine}} - E_{\text{MOF}} - E_{\text{amine}}, \tag{1}$$

where $E_{\text{MOF+amine}}$ is the energy of the MOF and a single amine, E_{MOF} is the energy of the non-functionalized MOF, and E_{amine} is the energy of the gaseous amine in a $28 \times 28 \times 28$ Å^3 super-cell.

We also consider the binding energy of a system when all of the OMS are bound (or at least blocked), deemed a fully functionalized pore. In this case, we average the binding energy over the number of amines in order to compare across materials, which may have different loadings. In this case, when there are N amines in the fully loaded pore, the binding energy is computed as

$$\Delta E_{\text{ads}} = \frac{1}{N}(E_{\text{MOF+N amines}} - E_{\text{MOF}} - N \times E_{\text{amine}}). \quad (2)$$

In the case of norspermine, which has two studied gaseous conformations, the considered E_{amine} is the energy of the conformation predicted for a given method.

The interaction energy between the binding of a single amine and a full pore can be quantified by observing a difference between the single amine binding and average amine binding. In cases where these values are approximately the same, one can suppose that there is little interaction energy. Larger discrepancies indicate an interaction energy that could make a given prediction less favorable in the presence of many amine molecules. Indeed, results in the next sections show that, in the case of the tetramines, the single amine binding energy does not always align with the prediction in the case of a fully loaded pore.

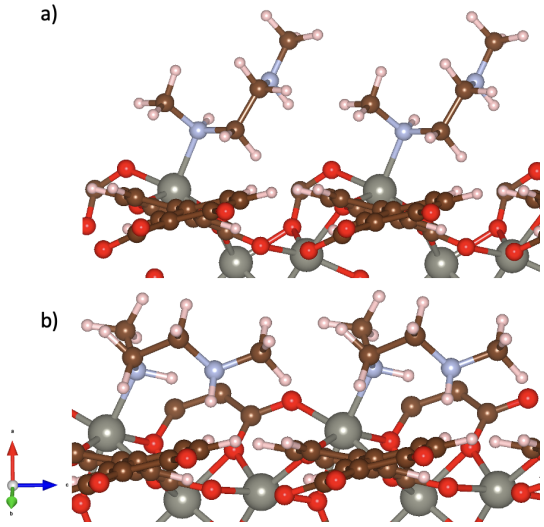

FIG. 1: Two different binding motifs for m2m: a) the *ab*-aligned configuration, wherein the ethylene-based arm is mostly in the *ab*-plane. b) the *c*-aligned configuration, wherein the ethylene-based arm is aligned along the crystallographic *c*-axis. Some of the linker molecules have been removed for visual clarity. The gray atoms are Zn, the red are O, the brown are C, the blue are N, and the white are H.

III. FUNCTIONAL AND DISPERSION CORRECTION DEPENDENCE OF BINDING AND LOADING

In the next three subsections (Sections III A, III B, III C), we present the predictions of the different functionals and van der Waals treatments on the loading and amine configuration, along with material-specific commentary. Higher-level commentary and interpretation of the results will be presented in Section IV.

Because some of the energy deltas approach degeneracy, we have to define some cutoff wherein if two configurations have an energy separation less than some value, we consider either of them possible. We set that value to 10 kJ/mol.

A. *N,N'*-dimethylethylenediamine

N,N'-dimethylethylenediamine, or m2m, is a diamine that that has one amine group coordinatively bound to an OMS and one amine group dangling in the pore (Figure 1). The singly-bound attachment generally gives this material more rotational freedom in the pore, making distinctions between its configuration somewhat blurrier than the tetramines we will discuss in the next section. In fact, there is evidence that there are multiple motifs that are energetically available at finite temperatures[34,65]. However, as in Lee, *et al.*, we take the 'true' ground state configuration to be the one in which the ethylene-based arm is parallel to the crystallographic *ab*-plane (Figure 1a). The alternate configuration is the one in which this ethylene arm is pointing in the direction of the crystallographic *c*-axis (Figure 1b).

TABLE I: Comparison of the predicted energies for the two different motifs, for a single amine and averaged over 6-amines in a full pore. A negative value indicates that the prediction is for the *ab*-aligned motif, the ground truth.

Calculation	1-amine $\Delta E_{b,ab} - \Delta E_{b,c}$ (kJ/mol)	6-amines $\Delta E_{b,ab} - \Delta E_{b,c}$ (kJ/mol)
PBE	-9	-21
PBE+GD2	-20	-21
PBE+GD3	-25	-21
PBEsol	-23	-20
PBEsol+GD2	-17	-24
PBEsol+GD3	-19	-21
revPBE+GD2	-7	-18
revPBE+GD3	-26	-18
RPBE+GD2	-8	-19
RPBE+GD3	-22	-18
vdW-DF2	-25	-19
NNP	-25	-8

Table I shows the difference in the binding energies for the *ab* and *c* motifs for m2m. Since there are only two motifs, we present the difference in the binding energies between the two configurations, both for a single amine and the fully-loaded pore of 6 amines, computed as described in Equations 1 and 2.

Inspection of Table I shows that all of the methods predict the correct configuration. However, at non-zero temperatures, one could argue that the single amine energy deltas for PBE (-9 kJ/mol), revPBE+GD2 (-7 kJ/mol), and RPBE+GD2 (-8

TABLE II: Comparison of the predicted binding motif for m2m-Zn_2(dobpdc) for different methods.

Calculation	1-amine prediction	6-amine prediction
PBE	*ab* or *c*	*ab*
PBE+GD2	*ab*	*ab*
PBE+GD3	*ab*	*ab*
PBEsol	*ab*	*ab*
PBEsol+GD2	*ab*	*ab*
PBEsol+GD3	*ab*	*ab*
revPBE+GD2	*ab* or *c*	*ab*
revPBE+GD3	*ab*	*ab*
RPBE+GD2	*ab* or *c*	*ab*
RPBE+GD3	*ab*	*ab*
vdW-DF2	*ab*	*ab*
NNP	*ab*	*ab* or *c*

kJ/mol) are small enough that one would consider both configurations. In the case of the full pore, all methods predict the correct configuration, though the NNP prediction approaches degeneracy with the true prediction only being 8 kJ/mol more favorable than the alternate motif. These predictions are qualitatively summarized in Table II.

What's interesting about this amine and configuration is that it is known to take multiple stable conformations at room temperature, as mentioned before. It is thus surprising to have such uniform agreement across the board for the different methodologies employed, given that even at 100K, there doesn't seem to be a single motif, but freedom of movement. There has been evidence of amine swapping reported, as well[65]. The *c*-aligned configuration, however, seems to suffer from strong enough steric repulsion along the *c*-axis that is unfavorable (without chemisorption of CO_2), meaning that it likely is not a physical motif.

B. *N,N'*-bis(3-aminopropyl)-1,3-diaminopropane

The next molecule we consider is the tetramine *N,N'*-bis(3-aminopropyl)-1,3-diaminopropane, henceforth called norspermine for succinctness. Norspermine has many conformations in the gaseous phase. We choose to study two main parent conformations, as show in Figure 2. These conformations are a subset of a large number of possible configurations, primarily owing to the flexibility of the alkyl chains and at the amine sites. The linear conformation of the molecule is what one would obtain were they to download the coordinates from ChemSpider[45], and so was explicitly considered here. Although one would not expect the tetramine to stay purely linear in the pore, due to energetic and geometric constraints, the nature of the bound norspermine in this conformation remains mostly linear, hence the terminology.

For each of these conformations, we draw the amine bound diagonally across the *ab*-plane and vertically, or column-bound, along the *c*-axis. See Figure 3. The S-shaped, diagonally bound motif is known to be the ground-state configuration, as reported in[19].

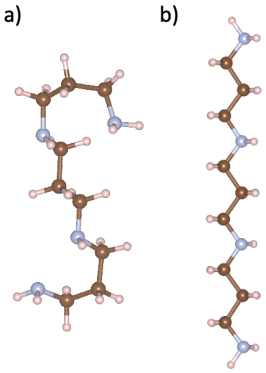

FIG. 2: The two different conformations of gaseous norspermine. a) is the 'S-shaped' conformation and b) is the linear one.

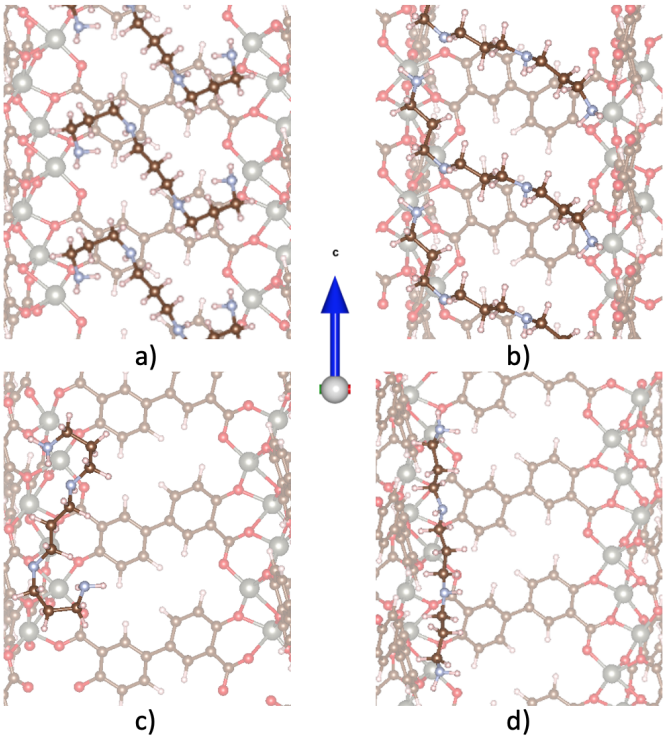

FIG. 3: The four different motifs studied for norspermine in the Zn_2(dobpdc) pore. a) is the S-shaped, diagonal (SD), to experimentally characterized motif. b) is the linear, diagonal (LD) motif. c) is the S-shaped, column (SC) motif. And d) is the linear, column (LC) motif.

While this known ground-state conformation looks somewhat perplexing and could be considered difficult to guess, the metal node-node distance in the unit cell of Zn_2(dobpdc) in the *ab*-plane is known to be about 10.4 Å, which aligns well with the 8.5 Å separation of the primary amines in norspermine. Indeed, performing a conformer search with Spartan[66] and constraining the terminal amine distance will discover the S-shaped configuration. Drawing a hypothetical functional-

TABLE III: Comparison of the predicted molecular conformation for norspermine. The negative value in $\Delta E_S - \Delta E_{\text{linear}}$ indicates that all methods predict a gaseous S-shaped conformation. As in the case of m2m, we do consider energy differences of less than 10 kJ/mol to approach degeneracy.

Calculation	Predicted conformation	$\Delta E_S - \Delta E_{\text{linear}}$ (kJ/mol)
PBE	S or linear	-8
PBE+GD2	S	-15
PBE+GD3	S	-12
PBEsol	S	-13
PBEsol+GD2	S or linear	-4
PBEsol+GD3	S	-17
revPBE+GD2	S or linear	-9
revPBE+GD3	S	-12
RPBE+GD2	S or linear	-9
RPBE+GD3	S	-11
vdW-DF2	S	-10
NNP	S	-14

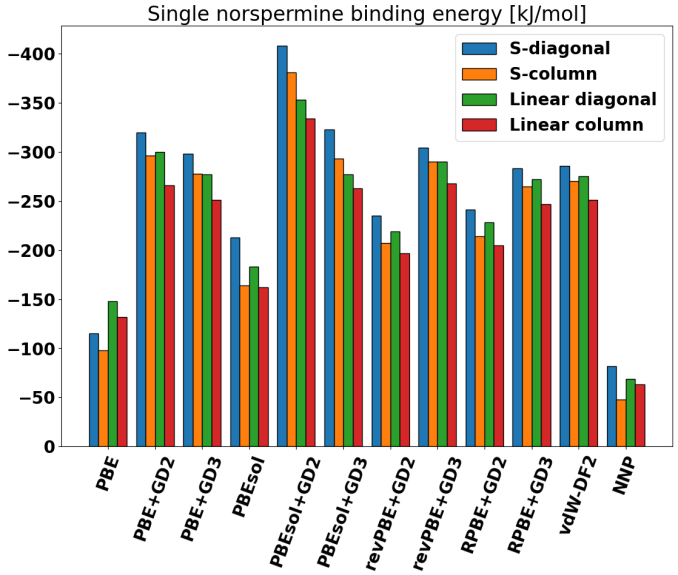

FIG. 4: A comparison of the calculated binding energies of a single norspermine attaching to the MOF for calculation schemes.

ized motif with unknown crystallographic structure is difficult, and knowledge of the base framework and amine must be incorporated.

In the linear, column-bound configuration, the geometry is such that there would be an uncapped metal site. These sites can cause increased water uptake[67], and therefore would generally want to be avoided. This motif has a different loading value. Amine loading is typically measured as the ratio of number of amines to the number of linkers. This value can be readily measured experimentally via NMR[19]. In the case of m2m, the loading is 2 diamines per linker. For norspermine, in the known configuration, the ratio is 1 tetramine per linker. The ratio holds for the linear, diagonally bound motif. It also holds for the column-bound S-shaped motif. For the column-bound linear motif, however, one would measure a loading of 2/3 (6 amines per 9 linkers, see image). Using this loading as the predicted value for amine screening would have you underestimate the capacity by about 33%, using the theoretical capacity of 2 CO_2 molecules per tetramine.

Figure 4 shows the computed binding energies across all of our calculation schemes for a single norspermine molecule attaching to the framework. A true ground-truth prediction would have the blue bar being the highest (most negative), which is true across all methods except regular PBE. The relatively large numbers compared to m2m and other diamines can be attributed to the fact that, for the most part, two bonds are forming: each primary amine is attaching to a Zn atom.

In PBE and PBEsol, we see the addition of the Grimme terms increases the binding strength substantially. Changing from GD2 to GD3 in the case of PBE and PBEsol decreases the binding strength, whereas it increases the binding strength for revPBE and RPBE. vdW-DF2 seems to most closely align with binding energy values of Grimme-D3. The NNP results most closely mimic the PBE values, though they do tend to under-bind in comparison. This alignment is likely due to NNP being primarily trained on PBE calculations in solids.

The more striking difference is in the substantial change of the S-column motif upon addition of the Grimme terms. It is very far from being as stable as the S-diagonal motif for PBE and PBEsol, but becomes much more favorable with the introduction of the dispersion corrections. Examination of the structures sheds some light on why this is the case, as shown in Figure 5. For PBE, the addition of the Grimme terms induces an attraction that allows for the amines to attach to two nodes, which is not the case in standard PBE. There is also clear formation of hydrogen bonds with the secondary amine and the oxygen backbone. For PBEsol, it is doubly-attached even in the absence of dispersion corrections. However, the geometry is such that formation of a stabilizing hydrogen bond is only allowed when including GD2 or GD3.

In the case of the full pore, the interaction energy plays a large role. The general width (and loss of surface area) in the S-shaped, column bound configuration makes it a much less likely conformation in a full pore. Adjacent S-shaped, column-bound amines became crowded and detached (or nearly so) at one site. There are also strong interaction energies between all configurations when the pore is full, except for the linear, column configuration. This can be attributed to the compact nature of amine in this motif, as seen in Figure 7 and the fact that the norspermine tends to have a position that is relatively unchanged between the single amine loading and the full pore.

Table IV presents a qualitative summary of the predicted binding motif for norspermine using the single-amine binding energy and the full pore, averaged binding energy. The differences in the functionals and how they alter the predictions will be discussed in more rigorous detail in Section IV. In the table, a shorthand is used to express the motifs, where the first letter is the amine conformation (S = S-shaped, L = linear)

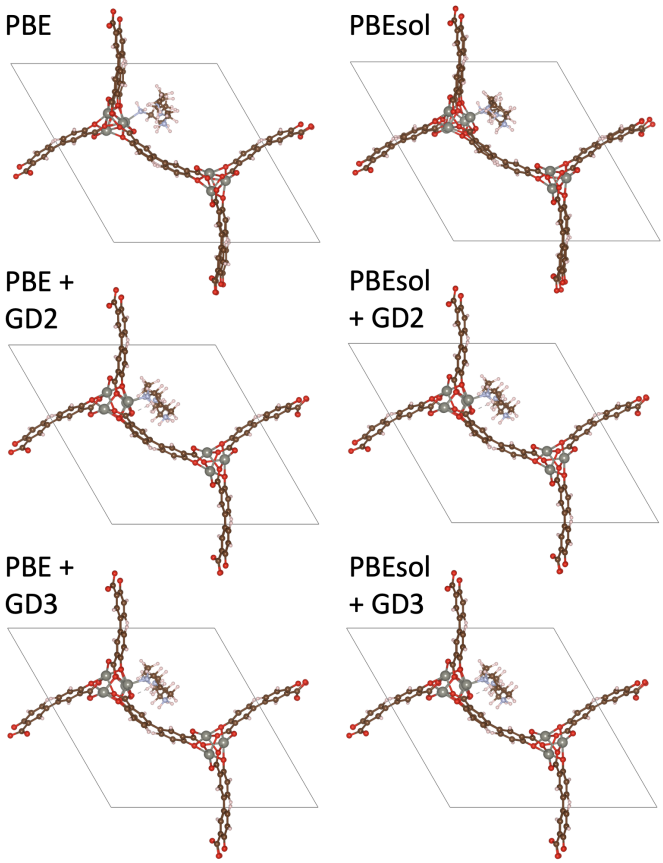

FIG. 5: View down the *c*-axis of a single S-shaped, column bound norspermine for PBE and PBEsol with different dispersion corrections, showing how the presence of such dispersion corrections bind this motif stronger, both via double amine attachment and hydrogen bonding on the backbone.

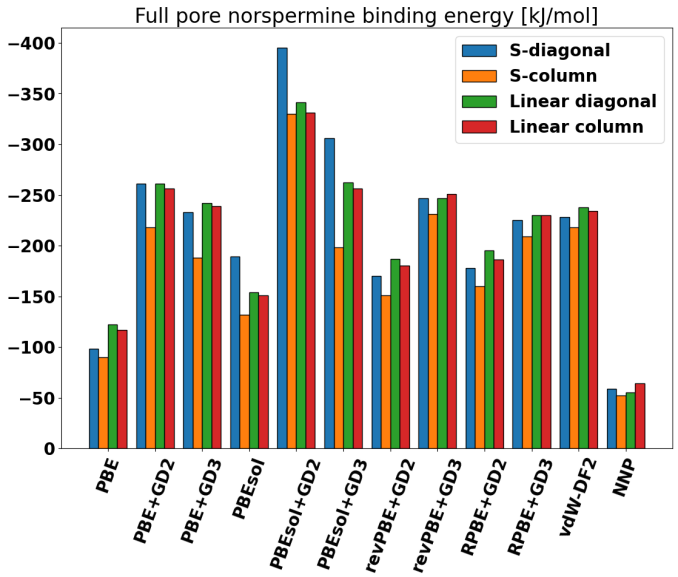

FIG. 6: A comparison of the calculated binding energies of a single norspermine attaching to the MOF for calculation schemes.

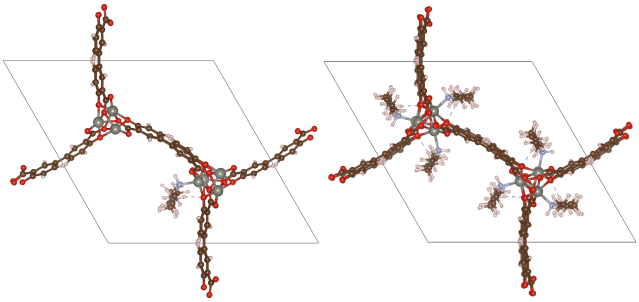

FIG. 7: A single linear, column-bound norspermine (left) and the full pore (right), displayed side-by-side to show how the amine does essentially no reconfiguring between these two scenarios, accounting for the low interaction energy.

and the second letter is the binding orientation (D = diagonal, C = column).

C. *N,N'*-bis(3-aminopropyl)-1,3-diaminobutane

The third species we study is *N,N'*-bis(3-aminopropyl)-1,3-diaminobutane, also called spermine. It is another tetramine and is known to be a particularly promising candidate for scalable deployment of carbon capture systems[19]. Spermine is very similar to norspermine. The difference is that the middle alkane between the secondary amines is butane instead of propane. This difference alters the length between the primary amines enough that it can span across three unit cell repetitions in the *c* direction, while retaining its linear character. See Figure 8.

The full pore motif predictions for spermine are unambiguously the experimentally characterized structure. The single amine binding energies tell a different story. One possible reason for this discrepancy is because the longer length of the center alkane chain (compared to norspermine) causes a buck-

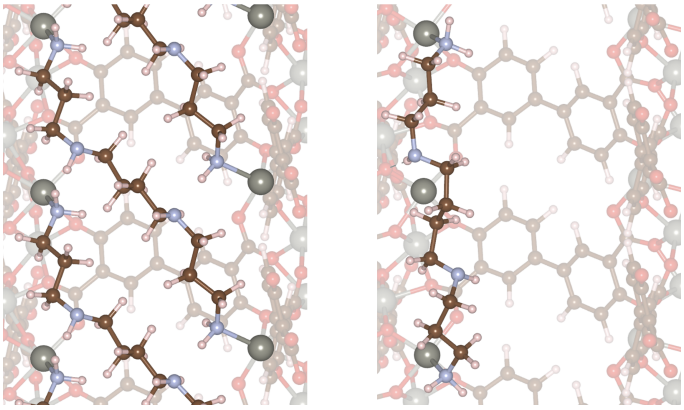

FIG. 8: Different binding motifs for spermine: diagonally bound (left), from the crystallographic structure and column-bound (right), a drawn motif. Notice the open metal sites in the column-bound configuration.

TABLE IV: Comparison of the predicted motifs for norspermine bound in the Zn_2(dobpdc) pore. A shorthand is used to express the predicted motif, wherein the first letter is the amine conformation and the second is its bound alignment in the pore. SD, for example, would be the S-shaped, diagonal alignment, etc.

Calculation	1-amine	Full-pore	Predicted loading
PBE	LD	LD | LC	1
PBE+GD2	SD	LD | SD | LC	1
PBE+GD3	SD	LD | LC | SD	1
PBEsol	SD	SD	1
PBEsol+GD2	SD	SD	1
PBEsol+GD3	SD	SD	1
revPBE+GD2	SD	LD | LC	1
revPBE+GD3	SD	LC | LD | SD	0.67
RPBE+GD2	SD	LD | LC	1
RPBE+GD3	SD	LD | LC | SD	1
vdW-DF2	SD	LD | LC | SD	1
NNP	SD	LC | SD | LD	0.67

TABLE V: Comparison of the predicted spermine binding energies for the two different motifs, for a single amine and averaged over 3 (or 6) amines in a full pore. A negative value indicates that the prediction is for the diagonally-aligned motif, the ground truth.

Calculation	Single tetramine $\Delta E_{b,d} - \Delta E_{b,c}$ (kJ/mol)	Full pore $\Delta E_{b,d} - \Delta E_{b,c}$ (kJ/mol)
PBE	10	-11
PBE+GD2	-13	-32
PBE+GD3	-2	-26
PBEsol	-6	-25
PBEsol+GD2	-31	-44
PBEsol+GD3	-17	-35
revPBE+GD2	7	-19
revPBE+GD3	4	-19
RPBE+GD2	7	-16
RPBE+GD3	4	-20
vdW-DF2	3	-16
NNP	-90	-88

ling in the column-bound configuration, forcing the molecule to expand in the *ab*-plane, thereby interacting with its column-bound neighbors in the full pore. The diagonally bound configuration is further stabilized by inter-molecular hydrogen bonding between adjacent molecules along the *c*-axis.

IV. DISCUSSION AND INTERPRETATION OF RESULTS

A. High-level summary

The notional results can be summarized by saying that all methods are able to properly predict the 'true' configuration for the diamine m2m, both in the case of a single amine and a full pore. For norspermine, the single amine calculations suggest a robustness in most of the methods, as they all predict the experimental configuration of S-shaped, diagonal except standard PBE. In the case of the full pore, interaction energies between adjacent amines come into play, complicating the predictions and only 3 out of 12 (25%) of the considered methods predict the experimental configuration. The situation is reversed for spermine: the single amine binding energies tend to predict a column-bound motif, while the full pore prediction is unanimously the diagonal conformation.

TABLE VI: Comparison of the predicted binding motif for spermine-Zn_2(dobpdc) for different methods.

Calculation	1-amine prediction	full pore prediction
PBE	C | D	D
PBE+GD2	D	D
PBE+GD3	D | C	D
PBEsol	D | C	D
PBEsol+GD2	D	D
PBEsol+GD3	D	D
revPBE+GD2	C | D	D
revPBE+GD3	C | D	D
RPBE+GD2	C | D	D
RPBE+GD3	C | D	D
vdW-DF2	C | D	D
NNP	D	D

As the full pore configurations correspond to the true structures, one would put more weight on a method's ability to properly account for amine-amine interaction, as well as amine-MOF interactions, when assessing the general accuracy of its predictions. With this logic, and ignoring possible degeneracy and just taking the lowest predicted configuration as the sole prediction, one would say that only PBEsol and PBEsol+GD2/3 all predict the loading and configuration correctly. This accounts for 3 out of the 12 considered calculation schemes, or 25%. If one were instead to only use the single amine binding as a quick screening, and again ignore possible degeneracy, PBE+GD2, PBE+GD3, PBEsol, PBEsol+GD2/3, and NNP would have accurate predictions of the full pore: 50%.

These results are summarized in Table VII. As above, in cases where the predictions are within 10 kJ/mol of each other, we do list all possible motifs. However, if the lowest energy one is still the correct one, we highlight it as green. If the lowest energy motif is different than the experimental one, we highlight it as yellow. If it is not in the same ballpark, we highlight it as red.

Although we have shown in Table VII that, across single amine and full pore predictions of amine motifs, PBEsol with or without Grimme dispersion corrections performs the best in terms of identifying the correct motif, the quantitative accuracy of this functional and dispersion correction(s) are different considerations. For example, while PBE gives the best binding enthalpy, revPBE and RPBE give the best overall compromise between the energetics and structural parameters[34].

Given these numbers, an appropriate screening pipeline for

TABLE VII: Summary qualitative comparison of the predicted binding motif for the different amines considered in this work for different density functionals and van der Waals treatments.

	1 m2m	1 NS	1 S	6 m2m	Full NS	Full S
PBE	*ab* | *c*	LD	C | D	*ab*	LC | LD	D
PBE+GD2	*ab*	SD	D	*ab*	LD | SD | LC	D
PBE+GD3	*ab*	SD	D | C	*ab*	LD | LC | SD	D
PBEsol	*ab*	SD	D | C	*ab*	SD	D
PBEsol+GD2	*ab*	SD	D	*ab*	SD	D
PBEsol+GD3	*ab*	SD	D	*ab*	SD	D
revPBE+GD2	*ab* | *c*	SD	C | D	*ab*	LD | LC	D
revPBE+GD3	*ab*	SD	C | D	*ab*	LC | LD | SD	D
RPBE+GD2	*ab*	SD	C | D	*ab*	LD | LC	D
RPBE+GD3	*ab*	SD	C | D	*ab*	LD | LC | SD	D
vdW-DF2	*ab*	SD	C | D	*ab*	LD | LC | SD	D
NNP	*ab*	SD	D	*ab*	LC | SD | LD	D

loading and motif determination would entail using the NNP for initial screening, and the higher accuracy calculations of PBEsol + GD3 could be used in the case of small energy deltas between full-pore motifs. Then, one could in principle use the methods that are known to be most accurate for their targeted application using the predicted motif.

B. Functional-specific discussions

Attempts to construct a better functional in the generalized gradient approximation (GGA) face a trade-off. Functionals with an enhanced gradient dependence improve atomization and total energies, but worsen bond lengths. Some suggestions of a GGA for solids have a reduced gradient dependence and typically do improve lattice parameters and/or surface energies, but have been criticized for worsening total and atomization energies. No GGA can do both: Accurate atomic exchange energies require violating the gradient expansion for slowly-varying densities, which is valid for solids and their surfaces[40].

The GGA form for the exchange energy is:

$$E_x^{GGA} = \int d^3r e_x^{LDA}(n(\boldsymbol{r}))F_x(s(\boldsymbol{r})). \tag{3}$$

Here, $n(\boldsymbol{r})$ is the electron density, $e_x^{LDA}(n(\boldsymbol{r}))$ is the exchange energy density of LDA, $s \propto |\bigtriangledown n|/n^{4/3}$ is the dimensionless density gradient, and $F_x(s)$ is the enhancement factor for the given GGA. This density gradient can be understand as being small in relatively uniform regions of electron density, but being larger in areas with greater variation in the electronic structure, such as surfaces. This physical understanding will be important as we decode the performance of the different functionals throughout this section.

For PBE and revPBE, this exchange enhancement factor has the form:

$$F_x(s) = 1 + \kappa - \frac{\kappa}{1 + \mu s^2/\kappa}. \tag{4}$$

μ and κ are constants. $\mu = \mu_{GE} = 10/81$ will recover the uniform electron gas, while, for PBE, $\mu = 2\mu_{GE}$ in order to approximate the exchange energies of neutral atoms.

RPBE slightly modifies the functional form of this enhancement factor:

$$F_x(s) = 1 + \kappa(1 - e^{-\mu s^2/\kappa}). \tag{5}$$

This change in functional form ensures that the RPBE functional satisfies the Lieb-Oxford bound, applicable as s gets larger[38]. In both cases, the $s \to 0$ limit, given by the Taylor expansion, is:

$$F_x(s) \approx 1 + \mu s^2, \tag{6}$$

meaning that the behavior in the slowly-varying density regions is the same.

Several suggestions explaining the reduction in the over-binding in GGA functionals have been put forward, the simplest of which is: (i) GGA functionals favor reduced density gradients, $s \propto |\bigtriangledown n|/n^{4/3}$; (ii) the volume of space with large s values scales with the free surface area, where "surface" may represent both a solid surface and the surface of molecules and atoms; (iii) a system with a molecule bound on a solid surface exposes less surface (and therefore has less volume with large s values) than do the reference systems of a clean solid surface and a gas phase molecule; (iv) consequently, the adsorption system is destabilized over the reference system. That is, the attachment will become less attractive and the binding energy will become less negative when using a GGA.

PBEsol's[40] tendency towards LDA-like behavior (as $\mu = \mu_{GE} = 10/81$ for PBEsol), and the demonstration of the LDA's large over-binding of adsorbates to transition-metal surfaces from[38] makes us expect it to over-bind relative to PBE. Indeed, this is observed in Figures 4 and 6. In addition, from Figures 2 and 3 of Hammer, Hansen, and Nørskov [38], revPBE and RPBE favor the reduced density gradients s, so that both revPBE and RPBE destabilize the adsorption system and give less attractive chemisorption energy. From Hammer, Hansen, and Nørskov [38] and Lee, Hyldgaard, and Neaton [34], we might expect the binding energy to follow the order to LDA $\sim$ PBEsol $>$ PBE $>$ revPBE $\sim$ RPBE. Although we didn't do plain revPBE and RPBE, we have shown that PBEsol and PBE follow this trend, and the GD2 correction applied to all four functions maintains this trend, too, for both the single amine and full pore cases.

This reasoning, from the perspective of the reduction of exposed surface area can also help understand the unexpected stability of the linear, column bound motif in the full pore norspermine, while the binding energy of a single norspermine in the pore predicts diagonal binding. Because it relates the stability of adsorption system to the amount of surface area

TABLE VIII: Comparison of the calculated accessible surface area (ASA) of different norspermine binding configurations in full pore loading from Zeo++ with 1.2 Å probe.

Motif	SD	SC	LD	LC
ASA [Å^2]	447	466	458	525

loss, and more loss of exposed surface will destabilize the adsorption system, from Figure 3, diagonally bound amines can fully cover the surface area of the DOBPDC linker, but the linear, column bound amines leave most of the linker surface area open.

In order to validate this, the accessible surface areas are calculated for all the different norspermine binding configurations in full-pore loading by Zeo++[68,69] with a 1.2 Å probe, shown in Table VIII. The SD, SC, and LD motifs all have similar surface areas, whereas the LC has one that is notably higher. This, along with the relatively small interaction energy in the linear, column-bound motif, can help explain its unexpected stability. This means when using GGA functionals, the diagonally bound amines destabilize the system more than the linear, column bound. On the other hand, when it comes to only absorbing 1 norspermine, the loss of surface area does not differ too much for different binding configurations, so that the column bound is never predicted to be close to the stability of SD or LD.

C. Dispersion corrections

The Grimme D2[41,60] dispersion correction is formulated as an additional contribution to the energy, accounting for the dipole-dipole interaction, and is mathematically defined as:

$$E_{\text{disp}} = -\frac{1}{2}\sum_{i=1}^{N_{\text{at}}}\sum_{j=1}^{N_{\text{at}}}\sum_{\mathbf{L}}\frac{C_{6ij}}{r_{ij,L}^{6}} f_{d,6}(r_{ij,\mathbf{L}}), \tag{7}$$

where the first two sums are over all N_{at} in the unit cell and the third summation is over all translations $\mathbf{L}$ of the unit cell, $i \neq j$ for $\mathbf{L} = 0$. C_{6ij} is the dispersion coefficient for atoms i and j. The values for C_{6ii} are parameterized for each element and are invariant to the chemical environment, meaning C_{6ii} for carbon in ethene is the same as carbon in ethane[60].

A modification of this method is called Grimme D3[42,60]:

$$E_{\text{disp}} = -\frac{1}{2}\sum_{i=1}^{N_{\text{at}}}\sum_{j=1}^{N_{\text{at}}}\sum_{\mathbf{L}}\left(\frac{C_{6ij}}{r_{ij,L}^{6}} f_{d,6}(r_{ij,\mathbf{L}}) + \frac{C_{8ij}}{r_{ij,L}^{8}} f_{d,8}(r_{ij,\mathbf{L}})\right). \tag{8}$$

There are two significant changes in the Grimme D3 scheme. The C_{6ii} coefficients are now geometry dependent: for each element, the value of C_{6ii} considers the coordination number. Second, there is the inclusion of an 8th order dispersion term. Generally speaking, the Grimme-D3 method is more accurate than Grimme-D2. As stated above, the reason we include Grimme-D2 in our analysis is because Quantum ESPRESSO does not yet have Grimme-D3 implemented for AIMD. Since we are interested in the thermal stability of our structures, support for AIMD is a requirement, so we also want to understand the performance of Grimme-D2 corrections.

The differences between the Grimme-type dispersion corrections (D2 and D3) are subtle, and can have many competing effects. While the GD3 scheme adds an additional energy term (R^8) (Equation 8), it does not always bind more strongly than GD2 (see Figures 4 and 6). The dispersion coefficients are different between GD2 and GD3, but, so are the damping functions used to force the dispersion correction to 0 at small atomic distances.

GD2 uses the Fermi damping function, defined as:

$$f_{\text{damp}}^{\text{Fermi}}(R) = \frac{1}{1 + e^{-20[R/s_r R_{\text{vdw}} - 1]}}, \tag{9}$$

where R is the ionic spacing, s_r is a functional-specific constant, and R_{vdW} is the sum of the van der Waals radii of to atoms.

GD3, by default in Quantum ESPRESSO, uses zero damping, for which the exact value depends on the R^6 term or R^8 term ($n = 6$ or $n = 8$, respectively):

$$f_{\text{damp,zero}}^{(n)}(R) = \frac{1}{1 + 6(R/(s_{r,n}R_0^{AB}))^{-a_n}}. \tag{10}$$

here R is the ionic spacing, $s_{r,n}$ is a functional-specific constant, R_0^{AB} is the species-specific vdW cutoff, and $a_n = 14, 16$ for $n = 6$ and $n = 8$, respectively. The exponential nature of Fermi damping makes it more aggressive at damping and thus the energetic contribution may fall off more rapidly at smaller distances. These considerations are in addition to the different correlation coefficients and the fact that Grimme D3 explicitly considers the atomic coordination number.

One interesting trend from Figure 6 is that the change from Grimme D2 to Grimme D3 decreases the magnitude of binding energy for PBE and PBEsol, but increases it for revPBE and RPBE. This is borne out it the numbers when you look at the dispersion contribution to the energy

Referring to Table VII, the change between GD2 and GD3 changes the nature of the predictions of the motif for the full pore of norspermine for PBE, revPBE, and RPBE. As such, these cases deserve some scrutiny. Table IX shows the contribution of the dispersion correction to the energy of the different systems, in units of meV/atom.

These numbers do make sense with the qualitative changes in the predictions. For PBE, interestingly enough, we see that the GD3 dispersion correction actually has smaller in magnitude energy contributions than GD2. This could happen based on the form of the different methods, as discussed above. As the SD motif becomes more favorable changing from GD2 to GD3, we see that the contribution of GD3 is larger in magnitude than for LD and LC, which qualitatively makes sense.

For revPBE and RPBE, the SD motif only becomes feasible when you switch from GD2 to GD3. Again, this makes sense based on the numbers in Table IX: SD has the largest change

TABLE IX: Comparison of the contribution to the total energy of the dispersion correction for full pore norspermine, for PBE, revPBE, RPBE, and vdW-DF2. Units are in meV/atom.

Calculation	SD	LD	LC
PBE+GD2	-69	-65	-63
PBE+GD3	-49	-46	-46
revPBE+GD2	-63	-61	-59
revPBE+GD3	-101	-96	-95
RPBE+GD2	-62	-60	-58
RPBE+GD3	-97	-93	-92
vdW-DF2	762	766	857

in magnitude (and becomes more negative) compared to LD and LC.

While the Grimme methods use a semi-empirical dispersion correction, there are other ways to account for the van der Waals interaction. One prominent method is to use a fully non-local functional, like vdW-DF2. In this formulation, the exchange correlation energy takes the form

$$E_{xc} = E_x^{GGA} + E_c^{LDA} + E_c^{nl}. \tag{11}$$

In this case, you have a non-local correlation term (E_c^{nl}), in addition to the GGA exchange and LDA correlation. This energy has a density-dependent kernel:

$$E_c^{nl}[n] = \frac{1}{2}\int d^3\mathbf{r}\int d^3\mathbf{r}' n(\mathbf{r})\Phi[n](\mathbf{r},\mathbf{r}')n(\mathbf{r}'). \tag{12}$$

This kernel has a complicated expression, with the presence of a spatial double integral[60]. In fact, the non-local energy contributions are positive for vdW-DF2, as seen in Table IX. The magnitude and trend of these numbers do not provide a clear understanding of the motif prediction for vdW-DF2. vdW-DF2, as compared to its predecessor vdW-DF1, changes the revPBE functional to the revised version of the PW86 functional[60]. Indeed, when compared with revPBE+GD2, we see that vdW-DF2 does bind the amines more favorably across the board. Its magnitude is similar, though, to revPBE+GD3. GD3 accounts more generally for interaction energies, as well, so both methods could be correcting similarly for the interaction energies. More studies are needed on the performance of non-local functionals.

V. THERMAL STABILITY

In addition to high capacity, fast sorption kinetics, and lower cost, thermal stability is a key requirement for a scalable and deployable CO_2 sorbent[70–73]. A quality sorbent must be thermally stable enough to withstand large numbers of adsorption and desorption cycles without losing chemical integrity or capacity[74,75]. In amine-functionalized MOFs, like we study here, thermal stability is especially important because the comparatively weaker coordination bonds that bind the amines to the framework are prone to detachment, exacerbated by thermal cycling and the adsorption/desorption process, and thus sorbent degradation, as the number of amines directly corresponds to CO_2 capacity.

TABLE X: Computed average binding energies of the crystallographically determined structures for each functional and dispersion correction. Units are in kJ/mol.

Calculation	Spermine	Norspermine	Prediction
PBE	-148	-98	S
PBE+GD2	-335	-261	S
PBE+GD3	-307	-233	S
PBEsol	-203	-89	S
PBEsol+GD2	-420	-395	S
PBEsol+GD3	-338	-306	S
revPBE+GD2	-228	-170	S
revPBE+GD3	-312	-247	S
RPBE+GD2	-234	-178	S
RPBE+GD3	-291	-225	S
vdW-DF2	-297	-228	S
NNP	-72	-59	S

The amine binding energy for the predicted motif could be used as a proxy for thermal stability and robustness to amine detachment, enabling the prediction of relative thermal stability between two amines. In Table X, we show the average binding energy (thus, coordination bond strength) of the known configurations for our battery of calculations. Spermine is generally thought to be more thermally stable[19], which is unanimously predicted by all calculations.

The above analysis hinges on the idea that a stronger coordination bond predicts a more thermally stable material. There is a trade-off, however: a weaker coordination bond between the amine and the metal nodes is also thought to be an indicator of allowing a CO_2 molecule to chemisorb easier, thereby lower the pressure at which the stepped adsorption takes place[65,76,77]. Further study is needed to quantitatively understand the trade-offs between these two effects.

In addition to the above analysis, the thermal stability of different motifs for norspermine is assessed via *ab initio* molecular dynamics and discussed in the Supplemental Material (Section VII A).

VI. CONCLUSIONS

The predictive landscape of the amine binding configuration of functionalized Mg_2(dobpdc) was explored using a variety of density functionals and dispersion corrections, as well as a neural network potential. PBEsol (with and without Grimme dispersion corrections) have the best performance in predicted the observed crystallographic motifs. We explored the reasons for these conclusions via analysis of properties of the different functionals considered. We demonstrated that calculations with a neural network potential and a single amine in the hypothesized motifs can reliably predict the binding configuration, and are appropriate for use as an

initial screening mechanism. Finally, we discussed the predicted strength of the coordination bond of the amine to the Zn nodes, and its proxy as an indicator of material thermal stability.

VII. SUPPLEMENTAL INFORMATION

A. Thermal stability via *ab initio* molecular dynamics

Molecular dynamics enables the simulation of atomic-scale events on a very fine time-scale, allowing for the study of rapid events like amine-detachment, at finite temperatures. In classical molecular dynamics, a force field typically represents a single potential energy surface, often the ground state, as a result of the Born–Oppenheimer approximation[78,79]. However, in cases involving excited states, chemical reactions, or when a more precise representation is required, electronic behavior can be derived from first principles using a quantum mechanical approach, such as density functional theory, leading to what is known as *ab initio* molecular dynamics (AIMD)[80,81]. *Ab initio* quantum mechanical and chemical techniques can be employed to dynamically calculate the potential energy of a system, particularly for conformations within a trajectory. These calculations, while potentially utilizing various approximations, are grounded in theoretical principles rather than empirical fitting. *Ab initio* computations yield extensive data that goes beyond what can be obtained through empirical methods, including information on electronic state densities and other electronic properties. Notably, one of the key advantages of employing *ab initio* methods is their capacity to investigate reactions involving the breaking or formation of covalent bonds, encompassing multiple electronic states. With recent advances in (AIMD) simulations and high performance computing systems[80], and the Car-Parrinello molecular dynamics (CPMD) framework[82] specifically, it is possible to study the dynamics of amine detachment.

All computations were conducted utilizing the Kohn-Sham Density Functional Theory (DFT) method in its plane wave/pseudopotential configuration, employing the CPMD code as implemented in Quantum ESPRESSO (QE)[83]. We selected the ultrasoft pseudopotentials[84] for this purpose, as required by the CPMD code implemented in QE. The input structures for the AIMD simulations were obtained from the previously optimized cells discussed in the main text section. Constant temperature AIMD simulations under the Car-Parrinello scheme[82] were performed and used Nose-Hoover chain thermostats[85,86] for the nuclei. Each system was carefully thermostatted to both 400K and 500K for a minimum duration of 1 picosecond (ps). These temperatures are chosen because it has been reported that the spermine or norspermine can be thermally stable up until approximately 500K[19]. A time step of 5 atomic units (au), equivalent to 0.121 femtoseconds (fs), was employed for integrating the equations of motion during both production and equilibration runs. In these calculations, an assumed mass of 700 atomic units (au) was used for the electrons. The Grimme D2 scheme was applied as an empirical correction to the AIMD energy, again due to the CPMD implementation in QE.

TABLE XI: Summary of qualitative comparison of the predicted thermal stability by showing the number of Zn-N bond breaks every 6 norspermine during AIMD runs for the different amine configurations of norspermine for different density functionals and dispersion corrections.

	T	LD	SD	LC	SC
PBE	400K	4	0	6	7
PBE	500K	4	4	6	7
PBE+GD2	400K	2	0	2	2
PBE+GD2	500K	2	0	6	2
PBEsol	400K	12	6	11	8
PBEsol	500K	10	8	11	10
PBEsol+GD2	400K	10	6	6	6
PBEsol+GD2	500K	10	8	9	9
revPBE+GD2	400K	0	2	3	/
revPBE+GD2	500K	4	4	4	/
RPBE+GD2	400K	2	2	2	/
RPBE+GD2	500K	4	2	5	/

In this work, the thermal stability of an AIMD run is quantitatively described by the number of Zn-N bond breaks per six norspermines, which can vary from 0 to 12. In this way, we can normalize the numbers since different motifs have different loadings/number of amines per unit cell. The results for the various norspermine motifs are shown in Table XI. For these runs, we want to determine if AIMD can help to find the correct amine motif when different motifs approach degeneracy based on their binding energy?

We say the MOF-amine system is more thermally stable if the number of Zn-N bonds that break are fewer. We look at both 400K and 500K. If one accounts for 500K being the ultimate indicator of a functional and dispersion correction's prediction of the most stable motif, we see that PBE+GD2, PBEsol, PBEsol+GD2, and RPBE+GD2 all predict the experimentally resolved motif as the most thermally stable.

B. N-Zn bond strength: stability vs. isotherm step location

As mentioned in the main text, other work has looked at the N-M (where M is one of Mg, Mn, Fe, Co, Ni, Cu, or Zn) bond strength as an indicator of the location of the step pressure in the isotherm[65,76,77]. A weaker bond allows for easier separation of the N and M atoms, thereby enabling CO_2 chemisorption at lower partial pressures. Shaidu *et al.* [77] point out that there is more nuance here, and that the binding enthalphies do not tell the whole story, and entropic effects must be included as a correction to the enthalpies, à la Gibbs free energy, are necessary for this description to fully correlate with the experimental data.

If one is thus interested in steps at lower partial-pressures, one would target materials that we have discussed as being less thermally stable. Further study is needed to understand the associated trade-offs.

VIII. ACKNOWLEDGEMENTS

This research used resources of the Oak Ridge Leadership Computing Facility at the Oak Ridge National Laboratory, which is supported by the Office of Science of the U.S. Department of Energy under Contract No. DE-AC05-00OR22725. This research used resources of the National Energy Research Scientific Computing Center (NERSC), a U.S. Department of Energy Office of Science User Facility located at Lawrence Berkeley National Laboratory, operated under Contract No. DE-AC02-05CH11231 using NERSC award ALCC-ERCAP0025949.

The authors would like to thank the many members of the decarbonization team at GE Vernova Advanced research for their insights and discussions.

IX. AUTHOR DECLARATIONS

A. Conflicts of interest

The authors have no conflicts to disclose.

B. Author contributions

JRO and BF conceptualized and designed the study, guided by discussions with DM and JL. JRO performed the initial motif drawing and the DFT calculations. BF generated full-pore structures, NNP relaxations, and the *ab initio* molecular dynamics runs. JRO and BF each contributed to the writing and qualitative and quantitative analysis of the results.

X. DATA AVAILABILITY STATEMENT

The data that support the findings of this study are available within the article and its supplementary material. This includes the fully relaxed CIF files for all studied motifs and functionals considered, CSV files with the amine binding energies, and a discussion on the initial *ab initio* molecular dynamics studies of thermal stability.

XI. REFERENCES

[1]A. R. Millward and O. M. Yaghi, "Metal-organic frameworks with exceptionally high capacity for storage of carbon dioxide at room temperature," Journal of the American Chemical Society **127**, 17998–17999 (2005), pMID: 16366539, https://doi.org/10.1021/ja0570032.

[2]K. Sumida, D. L. Rogow, J. A. Mason, T. M. McDonald, E. D. Bloch, Z. R. Herm, T.-H. Bae, and J. R. Long, "Carbon dioxide capture in metal–organic frameworks," Chemical Reviews **112**, 724–781 (2012), pMID: 22204561, https://doi.org/10.1021/cr2003272.

[3]J. Liu, P. K. Thallapally, B. P. McGrail, D. R. Brown, and J. Liu, "Progress in adsorption-based co2 capture by metal–organic frameworks," Chem. Soc. Rev. **41**, 2308–2322 (2012).

[4]T. A. Makal, J.-R. Li, W. Lu, and H.-C. Zhou, "Methane storage in advanced porous materials," Chem. Soc. Rev. **41**, 7761–7779 (2012).

[5]N. L. Rosi, J. Eckert, M. Eddaoudi, D. T. Vodak, J. Kim, M. O'Keeffe, and O. M. Yaghi, "Hydrogen storage in microporous metal-organic frameworks," Science **300**, 1127–1129 (2003), https://www.science.org/doi/pdf/10.1126/science.1083440.

[6]T. Qiu, Z. Liang, W. Guo, H. Tabassum, S. Gao, and R. Zou, "Metal–organic framework-based materials for energy conversion and storage," ACS Energy Letters **5**, 520–532 (2020), https://doi.org/10.1021/acsenergylett.9b02625.

[7]Y. Liu, L. Chen, L. Yang, T. Lan, H. Wang, C. Hu, X. Han, Q. Liu, J. Chen, Z. Feng, X. Cui, Q. Fang, H. Wang, L. Li, Y. Li, H. Xing, S. Yang, D. Zhao, and J. Li, "Porous framework materials for energy and environment relevant applications: A systematic review," Green Energy and Environment **9**, 217–310 (2024).

[8]H. D. Lawson, S. P. Walton, and C. Chan, "Metal–organic frameworks for drug delivery: A design perspective," ACS Applied Materials and Interfaces **13**, 7004–7020 (2021), pMID: 33554591, https://doi.org/10.1021/acsami.1c01089.

[9]S. M. Moosavi, A. Nandy, K. M. Jablonka, D. Ongari, J. P. Janet, P. G. Boyd, Y. Lee, B. Smit, and H. J. Kulik, "Understanding the diversity of the metal-organic framework ecosystem," Nature communications **11**, 1–10 (2020).

[10]"Climate Change: Atmospheric Carbon Dioxide," `https://www.climate.gov/news-features/understanding-climate/climate-change-atmospheric-carbon-dioxide`.

[11]X. Zhang, H. Zhao, Q. Yang, M. Yao, Y.-n. Wu, and Y. Gu, "Direct air capture of co2 in designed metal-organic frameworks at lab and pilot scale," Carbon Capture Science and Technology , 100145 (2023).

[12]V. M. Georgieva, E. L. Bruce, M. C. Verbraeken, A. R. Scott, W. J. Casteel Jr, S. Brandani, and P. A. Wright, "Triggered gate opening and breathing effects during selective co2 adsorption by merlinoite zeolite," Journal of the American Chemical Society **141**, 12744–12759 (2019).

[13]M. M. Lozinska, J. P. Mowat, P. A. Wright, S. P. Thompson, J. L. Jorda, M. Palomino, S. Valencia, and F. Rey, "Cation gating and relocation during the highly selective "trapdoor" adsorption of co2 on univalent cation forms of zeolite rho," Chemistry of Materials **26**, 2052–2061 (2014).

[14]T. M. McDonald, W. R. Lee, J. A. Mason, B. M. Wiers, C. S. Hong, and J. R. Long, "Capture of carbon dioxide from air and flue gas in the alkylamine-appended metal–organic framework mmen-mg2 (dobpdc)," Journal of the American Chemical Society **134**, 7056–7065 (2012).

[15]T. M. McDonald, J. A. Mason, X. Kong, E. D. Bloch, D. Gygi, A. Dani, V. Crocella, F. Giordanino, S. O. Odoh, W. S. Drisdell, *et al.*, "Cooperative insertion of co2 in diamine-appended metal-organic frameworks," Nature **519**, 303–308 (2015).

[16]T. Gelles, S. Lawson, A. A. Rownaghi, and F. Rezaei, "Recent advances in development of amine functionalized adsorbents for co 2 capture," Adsorption **26**, 5–50 (2020).

[17]A. C. Forse, P. J. Milner, J.-H. Lee, H. N. Redfearn, J. Oktawiec, R. L. Siegelman, J. D. Martell, B. Dinakar, L. B. Zasada, M. I. Gonzalez, *et al.*, "Elucidating co2 chemisorption in diamine-appended metal–organic frameworks," Journal of the American Chemical Society **140**, 18016–18031 (2018).

[18]P.-Q. Liao, X.-W. Chen, S.-Y. Liu, X.-Y. Li, Y.-T. Xu, M. Tang, Z. Rui, H. Ji, J.-P. Zhang, and X.-M. Chen, "Putting an ultrahigh concentration of amine groups into a metal–organic framework for co 2 capture at low pressures," Chemical science **7**, 6528–6533 (2016).

[19]E. J. Kim, R. L. Siegelman, H. Z. Jiang, A. C. Forse, J.-H. Lee, J. D. Martell, P. J. Milner, J. M. Falkowski, J. B. Neaton, J. A. Reimer, *et al.*, "Cooperative carbon capture and steam regeneration with tetraamine-appended metal–organic frameworks," Science **369**, 392–396 (2020).

[20]R. L. Siegelman, T. M. McDonald, M. I. Gonzalez, J. D. Martell, P. J. Milner, J. A. Mason, A. H. Berger, A. S. Bhown, and J. R. Long, "Controlling cooperative co2 adsorption in diamine-appended mg2 (dobpdc) metal–organic frameworks," Journal of the American Chemical Society **139**, 10526–10538 (2017).

[21]Z. Zhu, S. T. Parker, A. C. Forse, J.-H. Lee, R. L. Siegelman, P. J. Milner, H. Tsai, M. Ye, S. Xiong, M. V. Paley, *et al.*, "Cooperative carbon dioxide capture in diamine-appended magnesium–olsalazine frameworks," Journal of the American Chemical Society **145**, 17151–17163 (2023).

[22]P. J. Milner, R. L. Siegelman, A. C. Forse, M. I. Gonzalez, T. Runčevski, J. D. Martell, J. A. Reimer, and J. R. Long, "A diaminopropane-appended

metal–organic framework enabling efficient co2 capture from coal flue gas via a mixed adsorption mechanism," Journal of the American Chemical Society **139**, 13541–13553 (2017).

[23] J. Yong, R. Xie, Q. Huang, X. Zhang, B. Li, P. Xie, C. Wu, and L. Jiang, "Diamine-appended metal-organic framework for carbon capture from wet flue gas: Characteristics and mechanism," Separation and Purification Technology **328**, 125018 (2024).

[24] R. L. Siegelman, P. J. Milner, A. C. Forse, J.-H. Lee, K. A. Colwell, J. B. Neaton, J. A. Reimer, S. C. Weston, and J. R. Long, "Water enables efficient co2 capture from natural gas flue emissions in an oxidation-resistant diamine-appended metal–organic framework," Journal of the American Chemical Society **141**, 13171–13186 (2019).

[25] A. H. Berge, S. M. Pugh, M. I. Short, C. Kaur, Z. Lu, J.-H. Lee, C. J. Pickard, A. Sayari, and A. C. Forse, "Revealing carbon capture chemistry with 17-oxygen nmr spectroscopy," Nature Communications **13**, 7763 (2022).

[26] S. E. Ju, J. H. Choe, M. Kang, D. W. Kang, H. Kim, J.-H. Lee, and C. S. Hong, "Understanding correlation between co2 insertion mechanism and chain length of diamine in metal-organic framework adsorbents," ChemSusChem **14**, 2426–2433 (2021).

[27] H. Zhang, L.-M. Yang, and E. Ganz, "Unveiling the molecular mechanism of co2 capture in n-methylethylenediamine-grafted m2 (dobpdc)," ACS Sustainable Chemistry and Engineering **8**, 14616–14626 (2020).

[28] H. Zhang, C. Shang, L.-M. Yang, and E. Ganz, "Elucidation of the underlying mechanism of co2 capture by ethylenediamine-functionalized m2 (dobpdc)(m= mg, sc–zn)," Inorganic chemistry **59**, 16665–16671 (2020).

[29] J.-H. Lee, R. L. Siegelman, L. Maserati, T. Rangel, B. A. Helms, J. R. Long, and J. B. Neaton, "Enhancement of co 2 binding and mechanical properties upon diamine functionalization of m 2 (dobpdc) metal–organic frameworks," Chemical science **9**, 5197–5206 (2018).

[30] J. Kundu, J. F. Stilck, J.-H. Lee, J. B. Neaton, D. Prendergast, and S. Whitelam, "Cooperative gas adsorption without a phase transition in metal-organic frameworks," Physical review letters **121**, 015701 (2018).

[31] S. Choi, T. Watanabe, T.-H. Bae, D. S. Sholl, and C. W. Jones, "Modification of the mg/dobdc mof with amines to enhance co2 adsorption from ultradilute gases," The Journal of Physical Chemistry Letters **3**, 1136–1141 (2012).

[32] R. Stanton and D. J. Trivedi, "Investigating the increased co2 capture performance of amino acid functionalized nanoporous materials from first-principles and grand canonical monte carlo simulations," The Journal of Physical Chemistry Letters **14**, 5069–5076 (2023).

[33] A. C. Forse and P. J. Milner, "New chemistry for enhanced carbon capture: beyond ammonium carbamates," Chemical Science **12**, 508–516 (2021).

[34] J.-H. Lee, P. Hyldgaard, and J. B. Neaton, "An assessment of density functionals for predicting co2 adsorption in diamine-functionalized metal–organic frameworks," The Journal of Chemical Physics **156** (2022).

[35] A. D. Becke, "Density-functional exchange-energy approximation with correct asymptotic behavior," Physical review A **38**, 3098 (1988).

[36] J. P. Perdew, J. A. Chevary, S. H. Vosko, K. A. Jackson, M. R. Pederson, D. J. Singh, and C. Fiolhais, "Atoms, molecules, solids, and surfaces: Applications of the generalized gradient approximation for exchange and correlation," Physical review B **46**, 6671 (1992).

[37] J. P. Perdew, K. Burke, and M. Ernzerhof, "Generalized gradient approximation made simple," Physical review letters **77**, 3865 (1996).

[38] B. Hammer, L. B. Hansen, and J. K. Nørskov, "Improved adsorption energetics within density-functional theory using revised perdew-burke-ernzerhof functionals," Physical review B **59**, 7413 (1999).

[39] Y. Zhang and W. Yang, "Comment on "generalized gradient approximation made simple"," Physical Review Letters **80**, 890 (1998).

[40] J. P. Perdew, A. Ruzsinszky, G. I. Csonka, O. A. Vydrov, G. E. Scuseria, L. A. Constantin, X. Zhou, and K. Burke, "Restoring the density-gradient expansion for exchange in solids and surfaces," Physical review letters **100**, 136406 (2008).

[41] S. Grimme, "Semiempirical gga-type density functional constructed with a long-range dispersion correction," Journal of computational chemistry **27**, 1787–1799 (2006).

[42] S. Grimme, J. Antony, S. Ehrlich, and H. Krieg, "A consistent and accurate ab initio parametrization of density functional dispersion correction (dft-d) for the 94 elements h-pu," The Journal of chemical physics **132** (2010).

[43] K. Lee, É. D. Murray, L. Kong, B. I. Lundqvist, and D. C. Langreth, "Higher-accuracy van der waals density functional," Physical Review B **82**, 081101 (2010).

[44] C. Chen and S. P. Ong, "A universal graph deep learning interatomic potential for the periodic table," Nature Computational Science **2**, 718–728 (2022).

[45] "ChemSpider: Search and share chemistry," `https://www.chemspider.com/Chemical-Structure.70720.html`.

[46] "Avogadro: an open-source molecular builder and visualization tool. Version 1.20." `https://avogadro.cc/`.

[47] M. D. Hanwell, D. E. Curtis, D. C. Lonie, T. Vandermeersch, E. Zurek, and G. R. Hutchison, "Avogadro: an advanced semantic chemical editor, visualization, and analysis platform," Journal of cheminformatics **4**, 1–17 (2012).

[48] A. H. Larsen, J. J. Mortensen, J. Blomqvist, I. E. Castelli, R. Christensen, M. Dułak, J. Friis, M. N. Groves, B. Hammer, C. Hargus, E. D. Hermes, P. C. Jennings, P. B. Jensen, J. Kermode, J. R. Kitchin, E. L. Kolsbjerg, J. Kubal, K. Kaasbjerg, S. Lysgaard, J. B. Maronsson, T. Maxson, T. Olsen, L. Pastewka, A. Peterson, C. Rostgaard, J. Schiøtz, O. Schütt, M. Strange, K. S. Thygesen, T. Vegge, L. Vilhelmsen, M. Walter, Z. Zeng, and K. W. Jacobsen, "The atomic simulation environment—a python library for working with atoms," Journal of Physics: Condensed Matter **29**, 273002 (2017).

[49] P. Giannozzi, S. Baroni, N. Bonini, M. Calandra, R. Car, C. Cavazzoni, D. Ceresoli, G. L. Chiarotti, M. Cococcioni, I. Dabo, *et al.*, "Quantum espresso: a modular and open-source software project for quantum simulations of materials," Journal of physics: Condensed matter **21**, 395502 (2009).

[50] P. Giannozzi, O. Andreussi, T. Brumme, O. Bunau, M. B. Nardelli, M. Calandra, R. Car, C. Cavazzoni, D. Ceresoli, M. Cococcioni, *et al.*, "Advanced capabilities for materials modelling with quantum espresso," Journal of physics: Condensed matter **29**, 465901 (2017).

[51] P. Giannozzi, O. Baseggio, P. Bonfà, D. Brunato, R. Car, I. Carnimeo, C. Cavazzoni, S. De Gironcoli, P. Delugas, F. Ferrari Ruffino, *et al.*, "Quantum espresso toward the exascale," The Journal of chemical physics **152** (2020).

[52] H. J. Monkhorst and J. D. Pack, "Special points for brillouin-zone integrations," Physical review B **13**, 5188 (1976).

[53] A. Dal Corso, "Pseudopotentials periodic table: From h to pu," Computational Materials Science **95**, 337–350 (2014).

[54] "THEOS," `http://theossrv1.epfl.ch/Main/Pseudopotentials`.

[55] K. F. Garrity, J. W. Bennett, K. M. Rabe, and D. Vanderbilt, "Pseudopotentials for high-throughput dft calculations," Computational Materials Science **81**, 446–452 (2014).

[56] G. Prandini, A. Marrazzo, I. E. Castelli, N. Mounet, and N. Marzari, "Precision and efficiency in solid-state pseudopotential calculations," npj Computational Materials **4**, 72 (2018).

[57] L. Talirz, S. Kumbhar, E. Passaro, A. V. Yakutovich, V. Granata, F. Gargiulo, M. Borelli, M. Uhrin, S. P. Huber, S. Zoupanos, *et al.*, "Materials cloud, a platform for open computational science," Scientific data **7**, 299 (2020).

[58] G. Alonso, D. Bahamon, F. Keshavarz, X. Giménez, P. Gamallo, and R. Sayós, "Density functional theory-based adsorption isotherms for pure and flue gas mixtures on mg-mof-74. application in co2 capture swing adsorption processes," The Journal of Physical Chemistry C **122**, 3945–3957 (2018).

[59] A. Kundu, G. Piccini, K. Sillar, and J. Sauer, "Ab initio prediction of adsorption isotherms for small molecules in metal–organic frameworks," Journal of the American Chemical Society **138**, 14047–14056 (2016).

[60] S. Grimme, A. Hansen, J. G. Brandenburg, and C. Bannwarth, "Dispersion-corrected mean-field electronic structure methods," Chemical reviews **116**, 5105–5154 (2016).

[61] B. Vlaisavljevich, J. Huck, Z. Hulvey, K. Lee, J. A. Mason, J. B. Neaton, J. R. Long, C. M. Brown, D. Alfè, A. Michaelides, *et al.*, "Performance of van der waals corrected functionals for guest adsorption in the m2 (dobdc) metal–organic frameworks," The Journal of Physical Chemistry A **121**, 4139–4151 (2017).

[62] H. Wang, L. Zhang, J. Han, and W. E, "DeePMD-kit: A deep learning package for many-body potential energy representation and molecular dynamics," Comput. Phys. Comm. **228**, 178–184 (2018).

[63]S. Batzner, A. Musaelian, L. Sun, M. Geiger, J. P. Mailoa, M. Kornbluth, N. Molinari, T. E. Smidt, and B. Kozinsky, "E (3)-equivariant graph neural networks for data-efficient and accurate interatomic potentials," Nature communications **13**, 2453 (2022).

[64]A. Jain, S. P. Ong, G. Hautier, W. Chen, W. D. Richards, S. Dacek, S. Cholia, D. Gunter, D. Skinner, G. Ceder, *et al.*, "Commentary: The materials project: A materials genome approach to accelerating materials innovation," APL materials **1** (2013).

[65]J. Xu, Y. M. Liu, A. S. Lipton, J. Ye, G. L. Hoatson, P. J. Milner, T. M. McDonald, R. L. Siegelman, A. C. Forse, B. Smit, *et al.*, "Amine dynamics in diamine-appended mg2 (dobpdc) metal–organic frameworks," The journal of physical chemistry letters **10**, 7044–7049 (2019).

[66]"Spartan," `https://www.wavefun.com/downloads`.

[67]J. M. Kolle, M. Fayaz, and A. Sayari, "Understanding the effect of water on co2 adsorption," Chemical Reviews **121**, 7280–7345 (2021).

[68]T. F. Willems, C. H. Rycroft, M. Kazi, J. C. Meza, and M. Haranczyk, "Algorithms and tools for high-throughput geometry-based analysis of crystalline porous materials," Microporous and Mesoporous Materials **149**, 134–141 (2012).

[69]D. Ongari, P. G. Boyd, S. Barthel, M. Witman, M. Haranczyk, and B. Smit, "Accurate characterization of the pore volume in microporous crystalline materials," Langmuir **33**, 14529–14538 (2017).

[70]M. Ozkan, S. P. Nayak, A. D. Ruiz, and W. Jiang, "Current status and pillars of direct air capture technologies," Iscience (2022).

[71]A. Sodiq, Y. Abdullatif, B. Aissa, A. Ostovar, N. Nassar, M. El-Naas, and A. Amhamed, "A review on progress made in direct air capture of co2," Environmental Technology & Innovation **29**, 102991 (2023).

[72]X. Zhu, W. Xie, J. Wu, Y. Miao, C. Xiang, C. Chen, B. Ge, Z. Gan, F. Yang, M. Zhang, *et al.*, "Recent advances in direct air capture by adsorption," Chemical Society Reviews (2022).

[73]N. McQueen, K. V. Gomes, C. McCormick, K. Blumanthal, M. Pisciotta, and J. Wilcox, "A review of direct air capture (dac): scaling up commercial technologies and innovating for the future," Progress in Energy **3**, 032001 (2021).

[74]R. A. Khatri, S. S. Chuang, Y. Soong, and M. Gray, "Thermal and chemical stability of regenerable solid amine sorbent for co2 capture," Energy & Fuels **20**, 1514–1520 (2006).

[75]M. J. Lashaki, S. Khiavi, and A. Sayari, "Stability of amine-functionalized co 2 adsorbents: a multifaceted puzzle," Chemical Society Reviews **48**, 3320–3405 (2019).

[76]B. Vlaisavljevich, S. O. Odoh, S. K. Schnell, A. L. Dzubak, K. Lee, N. Planas, J. B. Neaton, L. Gagliardi, and B. Smit, "Co 2 induced phase transitions in diamine-appended metal–organic frameworks," Chemical science **6**, 5177–5185 (2015).

[77]Y. Shaidu, W. DeSnoo, A. Smith, E. Taw, and J. B. Neaton, "Entropic effects on diamine dynamics and co2 capture in diamine-appended mg2 (dopbdc) metal–organic frameworks," The Journal of Physical Chemistry Letters **15**, 1130–1134 (2024).

[78]D. Frenkel and B. Smit, *Understanding molecular simulation: from algorithms to applications* (Elsevier, 2023).

[79]M. P. Allen and D. J. Tildesley, *Computer simulation of liquids* (Oxford university press, 2017).

[80]D. Marx and J. Hutter, *Ab initio molecular dynamics: basic theory and advanced methods* (Cambridge University Press, 2009).

[81]G. Kresse and J. Hafner, "Ab initio molecular dynamics for liquid metals," Physical review B **47**, 558 (1993).

[82]R. Car and M. Parrinello, "Unified approach for molecular dynamics and density-functional theory," Physical review letters **55**, 2471 (1985).

[83]QuantumESPRESSO, "Cp'suserguide(v.7.2)," (2023).

[84]D. Vanderbilt, "Soft self-consistent pseudopotentials in a generalized eigenvalue formalism," Physical review B **41**, 7892 (1990).

[85]S. Nosé, "A molecular dynamics method for simulations in the canonical ensemble," Molecular physics **52**, 255–268 (1984).

[86]W. G. Hoover, "Canonical dynamics: Equilibrium phase-space distributions," Physical review A **31**, 1695 (1985).